Finite element analysis of composite forming at macroscopic and mesoscopic scale

Philippe Boisse, Naïm Naouar, Adrien Charmetant

Finite element analysis of composite forming at macroscopic and mesoscopic scale

Philippe Boisse, Naim Naouar, Adrien Charmetant,

Université de Lyon, INSA-Lyon, LaMCoS, F-69621 Lyon, France

Abstract

F.E. analyses of composite reinforcement forming are presented at macroscopic and mesoscopic scale. Simulations of 3D interlock fabric deformations are based on a hyperelastic model. The strain energy model uses the strain invariants representative to independent deformation modes of the interlock fabric. In a second part, a simulation at mescoscale of the deformation of a textile composite reinforcement is presented. The F.E. model is obtained from X-ray computed tomography of the fabric in order to be close to the real geometry. The advantage of such an approach in comparison to the use of a textile geometrical modeler is shown.

1 – Introduction.

R.T.M process produces high-performance composite parts by resin injection on a textile reinforcement made of continuous fibres (Advani, 1994; Ruiz *et al.,* 2011). This reinforcement, called preform, is shaped before resin injection. Complex shapes, in particular with double curvatures can be obtained by membrane deformations of the textile reinforcement. In plane shear angle is the main strain that allows to reach double curved shapes. Nevertheless all the shapes are not possible for a given reinforcement. Some defects can appear during forming such as wrinkles, gaps between the yarns, fracture of yarns …To avoid the costly development by try and error of these forming processes, the numerical

simulation can predict if the manufacturing process is possible and what are the conditions for a good achievement.

Two families of methods exist for fibrous reinforcement forming (or draping): kinematic and mechanical approaches. Kinematic models (fishnet algorithms) assume that the fibres are inextensible and that the reinforcement is mapped onto the surface of the component/forming tool by assuming that tow segments are able to freely shear at tow crossovers (Mark and Taylor, 1956; Van Der Ween, 1991). The mechanical behavior of the reinforcement, the exterior loads, sliding and friction on the tools are not taken into account. The main advantage of these methods is the small CPU times needed. On the other hand wrinkles and the effects of blank holders cannot be analyzed. The influence of the nature of the reinforcement cannot be analyzed either. The present chapter concerns mechanical approaches. The forming process is analyzed as a thermomechanical transformation of the composite submitted to displacements and temperature of the tools. The simulation needs an efficient mechanical law for the analyzed reinforcement or prepreg and an efficient finite element approach. The analysis is performed at finite strain. The mechanical behavior of the reinforcements is strongly influenced by its fibrous nature. The specificities of this behavior are summarized in section 2. Several specific models have been proposed (Rogers, 1989; Spencer, 2000; Yu *et al.,* 2002; Cao *et al.*, 2005; Ten Thije *et al.,* 2007; Khan *et al.,* 2010). A hyperelastic model for 3D fibrous reinforcements during forming is presented in section 3 (Charmetant *et al*, 2012). Textile reinforcements and prepregs present a clear multiscale structure. Forming simulations are generally made at macroscopic level. Section 4 present analyses of textile reinforcement deformation at mesoscopic scale i.e. at the scale of the representative unit cell. The finite element model is obtained from a X-ray computed tomography of the reinforcement.

2 – Specificities of composite material during forming

2.1. Different type of continuous fibre reinforcements

The composite reinforcements made up of continuous and discontinuous fibres must be distinguished. Injection processes (Fu *et al,* 2000; Eberhardt *et al,* 2001) or thermocompression processes (Le Corre *et al,* 2002) are possible in the case of short (discontinuous) fibres. Strongly loaded composite parts are made up of continuous fibres that are necessary to obtain high stiffness and high strength. The reinforcement can be made up of parallel juxtaposed fibres without interlacing (UD: unidirectional). This situation is the more favourable for stiffness in the fibre direction. The strength is quasi null in the transverse direction. This is a difficulty for forming process. A cohesion can be given to UD reinforcements by stitching. They are called Non Crimp Fabric (NCF) because the fibres are not undulated (Fig. 1a)(Yu *et al*, 2005; Lomov, 2011; Bel *et al*, 2012). Weaving is the classical way to assemble fibres that are gathered in warp and weft yarns and interlaced by weaving (Fig1b). 2D woven fabric are made up of a single layer of warp and weft yarns. In 3D fabric, the weaving concerns an important thickness and several layer of warp and weft yarns (Fig. 1c)(Mouritz *et al*, 1999; Dufour *et al*, 2014). In order to obtain a composite part with a given thickness, the UD, NCF and 2D woven reinforcement are stacked to form a laminate. These material can be subject to delamination. This is avoided by 3D weavings. Section 3 presents, a mechanical model for 3D composite reinforcement during forming and its application to the simulations of hemispherical drawing and large three point bending.

2.2. Different scales for composite reinforcement analysis

Composite reinforcements are made up of fibres usually gathered in yarns (3000 to 48000 fibres per carbon yarn). These yarns are themselves assembled by weaving or stitching. Three scales can be clearly distinguished for the analysis. These analyses can be made at the scale of the part (macroscopic scale), at the scale of the yarn (mesoscopic scale), or at the fibre scale

(microscopic scale). These three scales are simultaneously present in a reinforcement. The modelling and the simulations can be made at one of these three scale depending of the objective. Simulation of reinforcements or prepreg forming is usually done at macroscopic scale in order to determine the optimal conditions of a process, the directions of the fibres after forming and possibly the onset of defects (in particular wrinkling)(Pickett *et al,* 1995; Boisse *et al,* 1995; Hancock and Potter, 2005; Zouari *et al*, 2005; Jauffrès *et al,* 2010). The objectives of mesoscopic analyses include performing virtual tests on one or some representative elementary cells (Cai, 1992; Chen and Chou, 2000; Xue *et al*, 2005, Lomov et al 2007, Charmetant *et al,* 2011; Nguyen *et al*, 2013). They also permit to determine the properties of the deformed element cell, in particular the permeability of compacted or sheared reinforcements (Lekakou *et al,* 1996; Loix *et al,* 2008). Section 4 presents the use of X-ray computed tomography in order to build F.E. models for mesoscopic analyses that are as close as possible to the real reinforcement.

Analyses are also performed at the scale of the fibre (microscopic scale) (Zhou *et al*, 2004; Durville, 2010). At this scale the considered solids (here the fibres) are actually continuous. For upper scales (mesoscopic and macroscopic) the mechanical model must take into account the fibrous nature of the yarn or of the reinforcement that might be tricky. At the microscopic scale, the fibre can be seen as a beam. But there are many fibers in a yarn (several thousands) and much more in a preform. Microscopic scale analyses are presently limited to parts of reinforcements with moderate size.

3. Continuous approach for 3D composite forming process analysis

A hyperelastic constitutive law for 3D layer to layer angle interlock preforms is proposed. This model is macroscopic and aims to determine the strains and stresses of the whole 3D preform. The strain energy potential is defined for elementary deformation modes

3.1. Hyperelastic constitutive equation

The potential energy is a function that can be written as a function of the right Cauchy-Green strain tensor $\underline{\underline{C}}$:

$$w = w\left(\underline{\underline{C}}\right) \text{ with } \underline{\underline{C}} = \underline{\underline{F}}^T . \underline{\underline{F}} \tag{1}$$

The dependence of the strain energy potential on the material privileged directions can be introduced explicitly. Structural tensors representative of the anisotropy of the material are introduced. 3D interlock fabrics are made of warp and weft yarns which are perpendicular to each other in the initial configuration. The 3D material has three privileged directions: the warp direction $\underline{M}_1$, the weft direction $\underline{M}_2$ and a third direction $\underline{M}_3$, perpendicular to $\underline{M}_1$ and $\underline{M}_2$, (through the preform thickness). These directions define three structural tensors:

$$\underline{\underline{M}}_1 = \underline{M}_1 \otimes \underline{M}_1 ; \quad \underline{\underline{M}}_2 = \underline{M}_2 \otimes \underline{M}_2 \text{ and } \quad \underline{\underline{M}}_3 = \underline{M}_3 \otimes \underline{M}_3 \tag{2}$$

Taking (Boehler, 1978) into account, the strain energy density function of a hyperelastic law is written as:

$$w^{orth} = w^{orth}\left(I_1, I_2, I_3, I_{41}, I_{42}, I_{43}, I_{412}, I_{423}, I_{51}, I_{52}, I_{53}\right) \tag{3}$$

where I_1, I_2, I_3 are the invariants of $\underline{\underline{C}}$ defined by:

$$I_1 = Tr\left(\underline{\underline{C}}\right) \qquad I_2 = \frac{1}{2}\left(Tr\left(\underline{\underline{C}}\right)^2 - Tr\left(\underline{\underline{C}}^2\right)\right) \qquad I_3 = Det\left(\underline{\underline{C}}\right) \tag{4}$$

and where:

$$I_{4i} = \underline{\underline{C}} : \underline{\underline{M}}_i = \underline{M}_i \cdot \underline{\underline{C}} \cdot \underline{M}_i , \quad I_{4ij} = \underline{M}_i \cdot \underline{\underline{C}} \cdot \underline{M}_j \qquad I_{5i} = \underline{\underline{C}}^2 : \underline{\underline{M}}_i = \underline{M}_i \cdot \underline{\underline{C}}^2 \cdot \underline{M}_i \ (i = 1,3) \tag{5}$$

are the mixed invariants corresponding to the structural tensors.

The contribution of each deformation mode is assumed to be independent from the others, The strain energy density function is consequently the summation these contributions.

$$\frac{\partial w}{\partial \underline{\underline{C}}} = \sum_{i=1}^{n} \frac{\partial w_i}{\partial I_i} \frac{\partial I_i}{\partial \underline{\underline{C}}} \tag{6}$$

where I_i is the strain invariant of the i[th] deformation mode.

3.2. Physically based invariants.

A phenomenological approach is undertaken to build a physically motivated behavior law (Charmetant et al, 2012). Six deformation modes can be identified for a 3D composite reinforcement: in-plane shear, transverse shear in warp and weft directions, stretch in the weft and warp directions, and transverse compression. Each of this modes will be assigned a physical invariant (Fig. 3).The aim of this procedure is to ease the identification process.

The stretch invariants in warp and weft directions are defined using the I_{41} and I_{42}

$$I_{elong}^{\alpha} = \ln\left(\sqrt{I_{4\alpha}}\right) \qquad \alpha = 1,2 \tag{7}$$

The definition of the transverse compression invariant is more complex. This invariant is not only linked to the third direction $\underline{M}_3$. During a pure transverse shear solicitation for example, the length of the material vector $\underline{M}_3$ will not change but the thickness of the preform will decrease, The transverse compression invariant is consequently defined as the total volume change divided by the two yarn stretches:

$$I_{comp} = \frac{1}{2}\ln\left(\frac{I_3}{I_{41}I_{42}}\right) \tag{8}$$

The in-plane shear invariant can be linked to the angle variation γ between the material directions $\underline{M}_1$ and $\underline{M}_2$ in the initial configuration, and $\underline{m}_1$ and $\underline{m}_2$ in the current configuration. As $\underline{M}_1$ and $\underline{M}_2$ are perpendicular:

$$\sin(\gamma) = \frac{\underline{m}_1 \cdot \underline{m}_2}{\|\underline{m}_1\|\|\underline{m}_2\|} \tag{9}$$

Consequently, the in-plane shear invariant is defined by:

$$I_{cp} = \frac{I_{421}}{\sqrt{I_{41}I_{42}}} = \sin(\gamma) \tag{10}$$

As for the in-plane shear, the transverse shear invariants are defined by:

$$I_{ct\alpha} = \frac{I_{4\alpha 3}}{\sqrt{I_{4\alpha} I_{43}}} = \sin\left(\gamma_{\alpha 3}\right) \qquad (\alpha = 1,2) \tag{11}$$

The six deformation modes are assumed to be independent. The energy density is then defined as the summation of the contributions of the six deformation modes:

$$w(\underline{\underline{C}}) = \sum_{\beta=1}^{6} w_b(I_\beta) \tag{12}$$

The second Piola-Kirchhoff tensor is finally obtained by differentiation:

$$\underline{\underline{S}} = 2\sum \frac{\partial w_\beta}{\partial I_\beta} \frac{\partial I_\beta}{\partial \underline{\underline{C}}} \tag{14}$$

3.3. Strain energy potential identification

Tension in warp and weft direction tests are performed to identify the tensile potential. The transverse compaction strain energy density is identified from a compressive test. A bias extension test is performed to identify the in-plane shear properties. In this case a Levenberg–Marquardt algorithm is used to identify all the values. Finally a transverse shear test is used to identify the part of the strain energy that is coming from this deformation. Details of the identifications and the form given to the different potentials can be found in (Charmetant *et al*, 2012).

3.4 Simulation of a hemispherical forming of a 3D interlock reinforcement.

The hemispherical deep drawing test is frequently used to analyse fabric reinforcements forming experiments (Boisse *et al*, 1995; Yu *et al*, 2005; Jauffres *et al*, 2010). The hemisphere is doubly curved and in-plane strains of the fabric are necessary to obtain the shape. In-plane shear strains can cause wrinkles (Skordos *et al*, 2007 ; Boisse *et al*, 2011]. This wrinkles can be avoided thanks to blank holders that add tensions to the reinforcement (Lee *et al*, 2007; Boisse *et al*, 2011]. The

geometry of the tools of a hemispherical forming test are shown in Fig. 4. A drawbead locally compacts the preform creating tensile loads at the end of the forming to eliminate potential wrinkles. No wrinkles appear during the process (Fig. 5). The results of the simulation show the ability of the proposed hyperelastic 3D model to describe the behaviour of interlock reinforcements during forming. The shear angles obtained by the simulation (Fig. 5) are in good agreement with those measured on the experimental deformed shape. The transverse compaction strains are important under the drawbead. This is well described by the 3D simulation model (Fig. 5). These quantities are not provided when using standard shell finite elements.

3.5. Simulation of a three point bending of a 3D interlock reinforcement

As the fibre extensions are very small, bending of textile fabrics is a deformation which involves mainly transverse shear in a 3D model. The specificities of the deformations of interlock reinforcements are highlighted in a three point bending test (Fig. 6). The warp and weft yarns are oriented at 0°/90° in the test shown Fig. 6a and at ±45° in Fig. 6c.

In the case of the 0°/90° specimen, Fig. 6a shows that the cross sections remain close to vertical. The Euler–Bernoulli assumption (cross sections remain perpendicular to the mean line) is not verified. It is quite different when the yarns are oriented at ±45°. In this case, the cross sections remain approximately perpendicular to the mean line. The comparisons between the geometry obtained by simulations and experiments is made in Fig. 6a-6b and 6c-6d for the two yarn orientations. The simulation correctly describes the orientation of the cross sections relatively to the mean line (nearly vertical in Fig. 6a-6b when the yarns are oriented at 0°/90°; nearly perpendicular to the mean line when the yarns are oriented at ±45°). Some aspects of the simulations of bending of the interlock specimen are nevertheless less satisfactory. In particular at 0°/90°, the parts of the specimens external to the supports are almost aligned with the central part in the experiments. The simulations give nearly horizontal

external parts for this 0°/90° specimen. In addition the computed radius at the centre of the two specimens are smaller than in experiments.

3.6. Simulation of a three point bending of a 3D interlock reinforcement adding a local bending stiffness.

The differences between simulations based on the presented hyperelastic law and the experiments in three point bending are related to local fibre bending rigidity. The local bending stiffness of each fibre aims at keeping the external parts of the specimen aligned with the central part. In addition these local bending rigidities increase the central radius of the specimens. In the hyperelastic model presented above, as usual in classical continuum mechanics there is no local miscrostructure that permits to introduce volume couples. Generalized continuum mechanics approaches permit to model these couples (Forest, 1998 Maugin and Metrikine, 2010). In order to account for the fibre rigidities finite element beams are added to the 3D continuous hyperelastic material in the warp and weft directions. These beam elements bring the fibre bending stiffness. Fig. 7 shows the improvements obtain with this approach. The external parts of the specimen are almost aligned with the central part both in experiments and simulations. In addition the central radius of the specimen are in agreement with experiments. This shows that the microstructure and in particular the bending rigidity of the fibres should be taken into account in the mechanical behaviour of interlocks. Studies have been conducted or are in progress to propose models based on generalized continua (Ferretti *et al,* 2014, 2015; d'Agostino *et al,* 2015). However, the generalized continuum models are complex and difficult to identify and implement. For interlock forming simulation, the hyperelastic model described above and detailed in (Charmetant *et al*, 2012) may be an interesting compromise between accuracy and simplicity.

4. Simulation at the mesoscopic scale based on X-ray computed tomography analysis

The mesoscopic analyses, i.e. analyses at the scale of the yarn, can be used as virtual test to determine the mechanical properties of the reinforcement during forming. The influence of different parameters and in particular of the geometry of the yarns and of the weaving can be investigated without performing the experiments and consequently without manufacturing the considered reinforcement. In mesoscopic analysis, the geometry of the yarns, their contacts are described. But the fibres themselves are not modelled. The yarn is considered as a continuum. The behaviour of the yarn is specific since it is made of thousands of fibres which can slide with respect to each other. Different constitutive models have been proposed to describe the specificity of this yarn mechanical behavior. The mechanical behavior can be modelled by a hyperelastic law (Charmetant *et al*, 2011) or by a hypoelastic approach (Boisse *et al,* 2005; Badel *et al*, 2008). X-ray tomography offers a powerful tool allowing the exploration of the internal structure of the woven textile before and during its deformation. The technique used to obtain a F.E. model at mesoscopic scale is described in the present section (Naouar *et al*, 2014). A comparison is presented between experiments, simulations obtained from μCT and simulation based on an idealized geometry in the case of a transverse compression test of a carbon twill reinforcement.

4.1. Determination of the reinforcement geometry by X-ray computed tomography.

A laboratory tomograph is used to acquire 3D images of the reinforcement (Herman, 1980; Baruchel *et al*, 2000). As an example the analysis is performed on the Hexcel G0986® fabric (Fig. 8a). It is a 2x2 carbon twill. Its 3D reconstruction obtained by X-ray computed tomography is shown in Fig. 8. In order to define a finite element model of the representative unit cell (RUC) of the fabric an image segmentation is performed to separate warp and weft

yarns. A tomography cut is first obtained (Fig. 9). Orientations of the different part of the image are computed using the structure tensor J (Jahne, 1993, Jeulin and Moreaud, 2008):

$$J = \begin{bmatrix} \langle f_x, f_x \rangle_w & \langle f_x, f_y \rangle_w \\ \langle f_x, f_y \rangle_w & \langle f_y, f_y \rangle_w \end{bmatrix} \tag{15}$$

f_x and f_y are the partial derivatives of the image $f(x, y)$ relatively to x and y and

$$\langle g, h \rangle_w = \iint_{R^2} w(x, y) g(x, y) h(x, y) dxdy \tag{16}$$

$w(x, y) \geq 0$ is a weighting function that specifies the area of interest. The local orientation θ, the energy *E* and the coherency *C* are calculated from tensor J (Rezakhaniha *et al*, 2011).

$$\theta = \frac{1}{2} \arctan(2 \frac{\langle f_x, f_y \rangle_w}{\langle f_y, f_y \rangle_w - \langle f_x, f_x \rangle_w}) \tag{17}$$

$$E = Trace(J) = \langle f_x, f_x \rangle_w + \langle f_y, f_y \rangle_w \tag{18}$$

$$C = \frac{\lambda_{\max} - \lambda_{\min}}{\lambda_{\max} + \lambda_{\min}} = \frac{\sqrt{(\langle f_y, f_y \rangle_w - \langle f_x, f_x \rangle_w)^2 + 4 \langle f_x, f_y \rangle_w}}{\langle f_x, f_x \rangle_w + \langle f_y, f_y \rangle_w} \tag{19}$$

The pixels with higher energy values correspond to more anisotropic and more oriented materials. Coherency is 0 in case of isotropy and tends to 1 when anisotropy increases.
At each pixel, the orientation θ corresponds to a colour. In case of textile reinforcements, the two colours (blue and red) allow to separate warp and weft yarns (Fig. 9). Binarization and filter operations lead to two different grey levels for the parts of the image in the warp direction and for the parts in the weft direction (Fig 10). All the cuts are superimposed after these operations. Therefore the geometry of the woven reinforcement is obtained with separated warp and weft yarns (Fig. 10).

4.2. Woven cell mesh generation

Thanks to the segmentation step described above, the warp and weft yarns are separated. The marching cubes algorithm is used to define a polygonal surface by triangulating the external

surface of each yarn (Lorensen and Cline, 1987). A front algorithm (Jin and Tanner, 1993) is used to obtain a volume mesh of each yarn. The initial front is made up of the external triangles. Tetrahedral elements are generated step by step on the whole volume of the yarns (Fig. 11).

4.3. Mechanical behavior of the yarn

The equivalent continuum behaviour must take into account the fibrous nature of the material (Fig. 12). The fibre direction stiffness is much larger than the others. Consequently the constitutive tensor **C** is oriented by $\underline{\mathbf{f}}_1$ the unit vector in the direction of the fibre. The direction of the vector $\underline{\mathbf{f}}_1$ is in general not constant. Since it is a material direction, the initial fibre direction $\underline{\mathbf{f}}_1^0$ is transformed by $\underline{\underline{\mathbf{F}}}$, the gradient tensor, into $\underline{\mathbf{f}}_1$. An objective derivative defined from the fibre rotation is used for the fibrous yarns (Boisse *et al*, 2005; Badel *et al*, 2008).

$$\underline{\underline{\boldsymbol{\sigma}}}^{\nabla_\phi} = \underline{\underline{\underline{\underline{\mathbf{C}}}}} : \underline{\underline{\mathbf{D}}} \qquad \text{with} \qquad \underline{\underline{\boldsymbol{\sigma}}}^{\nabla_\phi} = \underline{\underline{\boldsymbol{\Phi}}} . \left(\frac{\mathrm{d}}{\mathrm{dt}} \left(\underline{\underline{\boldsymbol{\Phi}}}^{\mathrm{T}} . \underline{\underline{\boldsymbol{\sigma}}} . \underline{\underline{\boldsymbol{\Phi}}} \right) \right) . \underline{\underline{\boldsymbol{\Phi}}}^{\mathrm{T}} \quad (20)$$

where $\underline{\underline{\boldsymbol{\Phi}}}$ is the rotation of the fibre. It can be shown that this derivative is objective (Badel *et al*, 2008). The stress update is obtained as:

$$\left[\boldsymbol{\sigma}^{n+1}\right]_{f_i^{n+1}} = \left[\boldsymbol{\sigma}^{n}\right]_{f_i^{n}} + \left[\mathbf{C}^{n+1/2}\right]_{f_i^{n+1/2}} \left[\Delta\boldsymbol{\varepsilon}\right]_{f_i^{n+1/2}} \quad (21)$$

The rotation $\underline{\underline{\boldsymbol{\Phi}}}$ from the initial known frame $\{\underline{\mathbf{f}}_i^0\}$ to the current frame $\{\underline{\mathbf{f}}_i\}$ must be determined. From the transformation gradient $\underline{\underline{\mathbf{F}}}$, the current fibre direction $\underline{\mathbf{f}}_1$ can be determined. Assuming that the initial position of the fibre is $\underline{\mathbf{f}}_1^0$:

$$\underline{\mathbf{f}}_1 = \frac{\underline{\underline{\mathbf{F}}} . \underline{\mathbf{f}}_1^0}{\left\| \underline{\underline{\mathbf{F}}} . \underline{\mathbf{f}}_1^0 \right\|} \quad (22)$$

The other basis vectors $\underline{\mathbf{f}}_2$ and $\underline{\mathbf{f}}_3$ of the orthonormal frame $\{\underline{\mathbf{f}}_i\}$ are obtained from the material transformation of $\underline{\mathbf{f}}_2^0$:

$$\underline{\mathbf{f}}_2 = \frac{\underline{\underline{\mathbf{F}}}\,.\underline{\mathbf{f}}_2^0 - \left(\underline{\underline{\mathbf{F}}}\,.\underline{\mathbf{f}}_2^0.\underline{\mathbf{f}}_1\right)}{\left\|\underline{\underline{\mathbf{F}}}\,.\underline{\mathbf{f}}_2^0 - \left(\underline{\underline{\mathbf{F}}}\,.\underline{\mathbf{f}}_2^0.\underline{\mathbf{f}}_1\right)\right\|} \quad \text{and} \quad \underline{\mathbf{f}}_3 = \underline{\mathbf{f}}_1 \times \underline{\mathbf{f}}_2 \tag{23}$$

Then the rotation $\underline{\underline{\mathbf{\Phi}}}$ is obtained by:

$$\underline{\underline{\mathbf{\Phi}}} = \underline{\mathbf{f}}_i \otimes \underline{\mathbf{f}}_i^0 = \left(\underline{\mathbf{f}}_j\right)_i^0 \underline{\mathbf{f}}_i^0 \otimes \underline{\mathbf{f}}_j^0 = \left(\underline{\mathbf{f}}_j.\underline{\mathbf{f}}_i^0\right)\underline{\mathbf{f}}_i^0 \otimes \underline{\mathbf{f}}_j^0 \tag{24}$$

The constitutive matrix in equation (21) is written in the frame of the fibre and consequently it is directly in its specific form corresponding to the textile material under consideration. This constitutive matrix written in the fibre frame can be assumed constant in some cases. Generally it is not; the transverse behaviour of a fibrous yarn is depending on the strain state.

The strain field in the transverse section is partitioned in two parts. The "spherical" part represents the change of area of the yarn section, and the "deviatoric" part represents the change of shape of the yarn section.

$$[\tilde{\varepsilon}_T]_{f_i} = \begin{bmatrix} \varepsilon_s & 0 \\ 0 & \varepsilon_s \end{bmatrix} + \begin{bmatrix} \varepsilon_d & \varepsilon_{23} \\ \varepsilon_{23} & -\varepsilon_d \end{bmatrix} \tag{25}$$

with $\varepsilon_s = \dfrac{\varepsilon_{22} + \varepsilon_{33}}{2}$ et $\varepsilon_d = \dfrac{\varepsilon_{22} - \varepsilon_{33}}{2}$

From this decomposition the constitutive matrix of the material in the frame of the fibre is in the form (Badel *et al*, 2008b):

$$\left[\tilde{\tilde{C}}\right]_{f_i} = \begin{bmatrix} E & 0 & 0 & 0 & 0 & 0 \\ & \dfrac{A+B}{2} & \dfrac{A-B}{2} & 0 & 0 & 0 \\ & & \dfrac{A+B}{2} & 0 & 0 & 0 \\ & \textit{Symmetry} & & G & 0 & 0 \\ & & & & B & 0 \\ & & & & & G \end{bmatrix} \tag{26}$$

4.4. Mesoscopic analysis of the G986 reinforcement compaction based on the F.E. model obtained from the μCT

The material parameters of the hypoelastic law presented in section 4.3 can be identified by different elementary tests. A biaxial tensile test with k=1 i.e. with equal warp and weft strains (equibiaxial tensile test) is sufficient to determine all the parameters (Naouar *et al*, 2014). Actually, due to the weaving the yarn are much compacted in this test (Boisse *et al*, 2001). The simulation of the compaction of a Representative Unit Cell (RUC) is performed (Fig. 13, 14 and 15). Periodic boundary conditions were prescribed. The compaction behaviour is non-linear. The transverse stress versus fibre volume fraction V_f curve follows a classical "J" shape (Kelly, 2011). The result of the meso FE model built from μCT is compared to the experimental compaction (Fig. 15). The agreement is good.

A second F.E. model is considered. It is based the geometry obtained with the TexGen software (Long and Brown, 2011; TexGen, 2014). The transverse geometry of this model obtained with TexGen and of the model based on the X-ray computed tomography are compared in Fig. 13. The TexGen model is more regular. All the yarns have the same cross section. These sections are somewhat different when they are determined by X-ray computed tomography because of small imperfections. These geometrical models are used to build F.E. models and to simulate compaction (using the same behaviour law and parameters). The stress versus V_f curve obtained from the F.E. model based on the TexGen geometry is somewhat more stiff than in the case of the model based on X-ray μCT which is consistent with experiments. The idealized geometry is the reason for this stiffness increase. A strong interest of the F.E. models based on X-ray computed tomography is the possibility of taking into account the effective geometry of the yarns within the reinforcement. This real geometry is not well known when the reinforcement is complex, for instance in the case of 3D or interlock fabrics.

5. Conclusions

The fibrous nature of composite reinforcements gives them a specific mechanical behavior. The F.E. simulations of their deformation can avoid the development of forming processes by try and error. The simulations can be made at macroscopic, mesoscopic and possibly microscopic scale. Simulations of composite reinforcement forming processes are usually performed at macroscopic scale. Shell finite elements are generally used to model each ply of the laminate. For 3D reinforcements, 3D finite elements are necessary. A hyperelastic model for these 3D analyses has been presented. It is based on the physical deformation modes of the 3D reinforcements. It has shown to be able to describe the specific mechanical behavior of 3D interlock reinforcements in three point bending. The cross section of the specimen remains nearly vertical for a 0/90° orientation of the yarns but are perpendicular to the mean line in the case of a ±45° orientation. This is well depicted by the hyperelastic model. Nevertheless some aspects of the deformation would require a generalized mechanics approach to take into account the local bending stiffness of the fibres.

At the mesoscopic scale, the F.E. simulation gives the deformation of the internal textile reinforcement structure. The analysis is usually made on a representative woven cell or on a few of them. Probably in the future it can concern a whole preform. The result of the simulation mainly depends on the quality of the initial F.E. model. X-Ray tomography is a possible way to define meshes close to the real reinforcement. This approach will be particularly interesting in the case of 3D fabrics for which geometry is complex and not always well known.

References

Advani SG (1994). *Flow and rheology in polymeric composites manufacturing*. Elsevier Amsterdam.

Badel P, Vidal-Sallé E, Boisse P (2008). Large deformation analysis of fibrous materials using rate constitutive equations, *Computers and Structures*, 86 (11–12): 1164‑1175.

Badel P, Vidal-Salle E, Maire E, Boisse P (2008b). Simulation and tomography analysis of textile composite reinforcement deformation at the mesoscopic scale. *Compos Sci Technol,* 68(12): 2433–40.

Baruchel J, Buffiere JY, Maire E, Merle P, Peix G (2000). *X-Ray Tomography in Material Science*. Baruchel J, Buffiere J., Maire E, Merle P, Peix G, editors. Hermes Science,

Bel S, Hamila N, Boisse P, Dumont F (2012). Finite element model for NCF composite reinforcement preforming: Importance of inter-ply sliding. *Composites Part A*, 43 (12): 2269–2277.

Boisse P, Cherouat A, Gelin JC, Sabhi H (1995). Experimental Study and Finite Element Simulation of Glass Fiber Fabric Shaping Process. *Polymer Composites*, 16(1): 83-95.

Boisse P, Gasser A, Hivet G (2001). Analyses of fabric tensile behaviour: determination of the biaxial tension–strain surfaces and their use in forming simulations. *Composites Part A.* 32 (10), 1395-1414

Boisse P, Gasser A, Hagège B, Billoet JL (2005). Analysis of the mechanical behavior of woven fibrous material using virtual tests at the unit cell level. *J. Mater. Sci*., 40 (22): 5955‑5962.

Boisse P, Hamila N, Vidal-Sallé E, Dumont F (2011). Simulation of wrinkling during textile composite reinforcement forming. Influence of tensile in-plane shear and bending stiffnesses. *Composites Science and Technology*, 71 (5): 683–92.

Boehler JP (1978). Lois de comportement anisotropes des milieux continus. *J Méc*, 17:153–70.

Cai Z, Gutowski T (1992). The 3-D deformation behavior of a lubricated fiber bundle. *J Comp Mater*, 26:1207-37.

Charmetant A, Vidal-Salle E, Boisse P (2011). Hyperelastic modelling for mesoscopic analyses of composite reinforcements. *Composites Science and Technology*, 71(14): 1623–1631

Charmetant A, Orliac JG, Vidal-Sallé E, Boisse P (2012). Hyperelastic model for large deformation analyses of 3D interlock composite preforms, *Composites Science and Technology*, 72 (12): 1352‑1360

Chen B, Chou TW (2000). Compaction of woven-fabric preforms: nesting and multi-layer deformation. *Composites Science and Technology*, 60: 2223-2231

Dufour C, Wang P, Boussu F, Soulat D (2014). Experimental Investigation about Stamping Behaviour of 3D Warp Interlock Composite Preforms. *Appl Compos Mater* 21:725–738.

Durville D (2010). Simulation of the mechanical behaviour of woven fabrics at the scale of fibers, *Int J Mater Form,* 3 (2): 1241–1251

Eberhardt C, Clarke A, Vincent M, Giroud T, Flouret S (2001). Fibre-orientation measurements in short-glass-fibre composites II: a quantitative error estimate of the 2D image analysis technique. *Composites Science and Technology*, 61 (13): 1961–1974.

Ferretti M, Madeo A, dell'Isola F, Boisse P (2014), Modeling the onset of shear boundary layers in fibrous composite reinforcements by second-gradient theory*, Zeitschrift für angewandte Mathematik und Physik*, 65, (3): 587-612

Forest S (1998). Cosserat overall modeling of heterogeneous materials. *Mechanics Research Communications,* 25: 449-454

Fu SY, Lauke B, Mäder E, Yue CY, Hu X (2000). Tensile properties of short glass fiber and short carbon fiber reinforced polypropylene composites; *Composites part A*, 31 (10): 1117–1125.

Hancock SG, Potter KD (2005). Inverse drape modelling - an investigation of the set of shapes that can be formed from continuous aligned woven fibre reinforcements. *Composites: Part A*, 36: 947-53.

Herman GT(1980). *Image Reconstruction from Projections: The Fundamentals of Computerized Tomography*. Herman GT, editor. New York: Academic Press.

Jahne B (1993). *Spatio-temporal image processing: Theory and scientific applications.* Jahne B, editor. Springer.

Jauffrès D, Sherwood JA, Morris CD, Chen J (2010). Discrete mesoscopic modeling for the simulation of woven-fabric reinforcement forming, *Int J Mater Form*, 3: 1205-16.

Jeulin D, Moreaud M (2008). Segmentation of 2d and 3d textures from estimates of the local orientation. *Image Analysis & Stereology*. 27: 183‑92. Jin H, Tanner R (1993).

Generation of unstructured tetrahedral meshes by advancing front technique. *International Journal for Numerical Methods in Engineering*, 36(11):1805‑23.

Khan MA, Mabrouki T, Vidal-Sallé E, Boisse P (2010). Numerical and experimental analyses of woven composite reinforcement forming using a hypoelastic behaviour. Application to the double dome benchmark. *J Mater Process Technol*, 210:378–88.

Kelly P (2011). Transverse compression properties of composite reinforcements. *Composite reinforcements for optimum performance*. Woodhead Publishing: 333‑366.

Laure P, Silva L, Vincent M (2011). Modelling short fibre polymer reinforcements for composites *in Composite reinforcements for optimum performance*. Woodhead Publishing Limited, 616-647.

Le Corre S, Orgéas L, Favier D, Tourabi A, Maazouz A, Venet V (2002). Shear and compression behaviour of sheet moulding compounds. *Composites Science and Technology*, 62 (4): 571–577.

Lee J, Hong S, Yu W, Kang T (2007). The effect of blank holder force on the stamp forming behaviour of non-crimp fabric with a chain stitch. *Compos Sci Technol,* 67:357–66.

Lekakou C, Johari MAKB, Bader MG (1996). Compressibility and flow permeability of two-dimensional woven reinforcements in the processing of composites, *Polymer Composites*, 17 (5): 666-672.

Loix F, Badel P, Orgéas L, Geindreau C, Boisse P (2008). Woven fabric permeability: from textile deformation to fluid flow mesoscale simulations. Composites Science and Technology, 68: 1624–1630

Lomov SV, Ivanov DS, Verpoest I, Zako M, Kurashiki T, Nakai H, Hirosawa S (2007). Meso-FE modelling of textile composites: Road map, data flow and algorithms. *Composites Science and Technology,* 67: 1870–1891.Lomov SV (2011) Ed. *Non-Crimp Fabric Composites: Manufacturing, Properties and Applications,* Woodhead Publishing Limited.

Long AC, Brown LP (2011), Modelling the geometry of textile reinforcements for composites: TexGen. *Composite reinforcements for optimum performance*. Woodhead Publishing: 239-264.

Lorensen WE, Cline HE (1987). Marching cubes: A high resolution 3D surface construction algorithm. *Proceedings of the 14th annual conference on Computer graphics and interactive techniques*. ACM, New York, NY, USA:163‑9

Madeo A, d'Agostino MV, Giorgio I, Greco L, Boisse P (2015). Continuum and discrete models for structures including (quasi-)inextensible elasticae with a view to the design and modeling of composite reinforcement. *Int J Sol Struct*, in press.

Madeo A, Ferretti M, dell'Isola F, Boisse P (2015). Thick fibrous composite reinforcements behave as special second gradient materials: three point bending of 3D interlocks, *Zeitschrift für angewandte Mathematik und Physik*, in press.

Mark C, Taylor HM (1956). The fitting of woven cloth to surfaces, *Journal of Textile Institute*, 47: 477-488.

Maugin GA, Metrikine V (eds) (2010). Mechanics of Generalized Continua: One hundred years after the Cosserats, *Advances in Mechanics and Mathematics* 21, Springer.

Mouritz AP, Bannister MK, Falzon PJ, Leong KH (1999), Review of applications for advanced three-dimensional fibre textile composites, *Composites Part A,* 30: 1445–1461.

Naouar N, Vidal-Sallé E, Schneider J, Maire E, Boisse P (2014). Meso-scale FE analyses of textile composite reinforcement deformation based on X-ray computed tomography, *Composite Structures*, Volume 116: 165–176.

Nguyen QT, Vidal-Sallé E, Boisse P, Park CH, Saouab A, Breard J, Hivet G (2013). Mesoscopic scale analyses of textile composite reinforcement compaction, *Composites Part B* 44 (1): 231–241

Peng XQ, Cao J (2005). A continuum mechanics-based non-orthogonal constitutive model for woven composite fabrics. *Composites part A*, 36 (6): 859–874.

Pickett AK, Queckbörner T, De Luca P, Haug E (1995). An explicit finite element solution for the forming prediction of continuous fibre-reinforced thermoplastic sheets. *Compos Manuf,* 6 (3–4): 237–43

Rezakhaniha R, Agianniotis A, Schrauwen JTC, Griffa A, Sage D, Bouten CVC, van de Vosse FN, Unser M, Stergiopulos N (2011). Experimental investigation of collagen waviness and orientation in the arterial adventitia using confocal laser scanning microscopy. *Biomechanics and Modeling in Mechanobiology*, 11(3- 4): 461–473,

Rogers TG (1989). Rheological characterization of anisotropic materials, *Composites*, 20 (1): 21–27

Ruiz E, F. Trochu (2011). Flow modeling in composite reinforcements *in Composite reinforcements for optimum performance*, Woodhead Publishing Limited, 588-615.

Skordos AA, Monroy Aceves C, Sutcliffe MPF (2007). A simplified rate dependent model of forming and wrinkling of pre-impregnated woven composites. *Composites Part A*, 38:1318–30.

Spencer AJM (2000). Theory of fabric-reinforced viscous fluids. *Composites Part A*, 31: 1311–1321

Ten Thije RHW, Akkerman R, Huétink J (2007). Large deformation simulation of anisotropic material using an updated Lagrangian finite element method. Comput Methods Appl Mech Eng, (196): 3141–50.

TexGen (2014). Available from: http://texgen.sourceforge.net/index.php/Main_Page (accessed 15 December 2014)

Van Der Ween F (1991). Algorithms for draping fabrics on doubly curved surfaces. *International Journal of Numerical Method in Engineering*, 31: 1414-1426.

Xue P, Cao J, Chen J (2005). Integrated micro/macro-mechanical model of woven fabric composites under large deformation. *Composite Structures,* 70: 69–80

Yu WR, Pourboghrat F, Chung K, Zamploni M, Kang TJ (2002). Non-orthogonal Constitutive Equation for Woven Fabric Reinforced Thermoplastic Composites. *Composites Part A.* 33: 1095-1105.

Yu WR, Harrison P, Long A (2005). Finite element forming simulation for non-crimp fabrics using a non-orthogonal constitutive equation. *Composites: Part A*, 36:1079–93.

Zhou G, Sun X, Wang Y (2004). Multi-chain digital element analysis in textile mechanics. *Compos Sci Technol*, 64:239–44.

Zouari B, Daniel JL, Boisse P (2006). A woven reinforcement forming simulation method. Influence of the shear stiffness. *Computers and Structures,* 84 (5-6): 351-363.

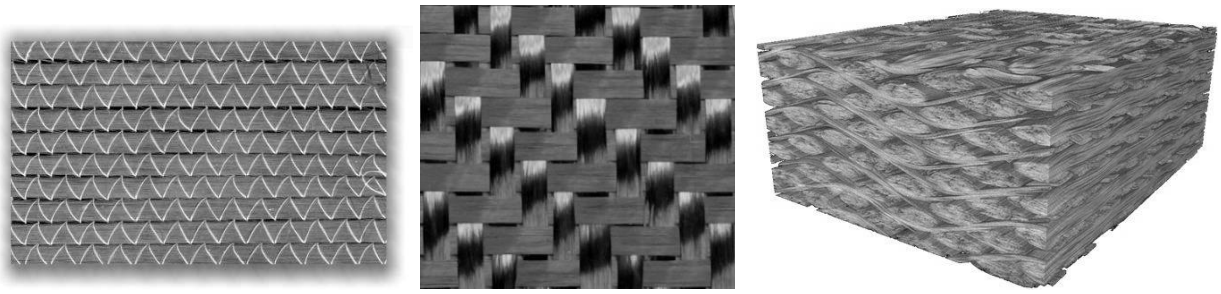

Fig. 1. NCF, woven and 3D reinforcements

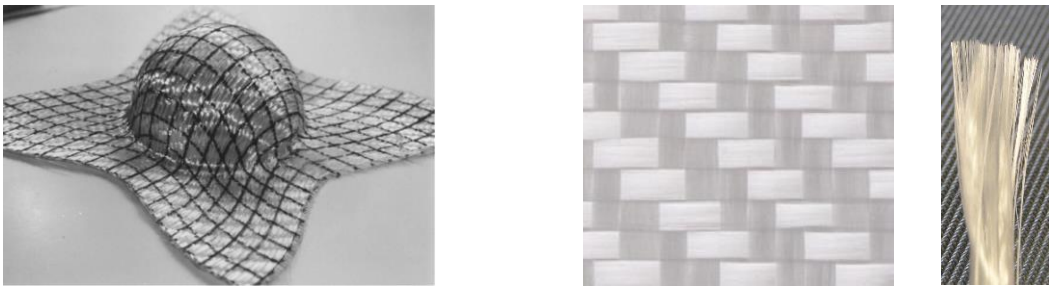

Fig. 2. Macroscopic scale (left); mesoscopic scale (middle); microscopic scale (right)

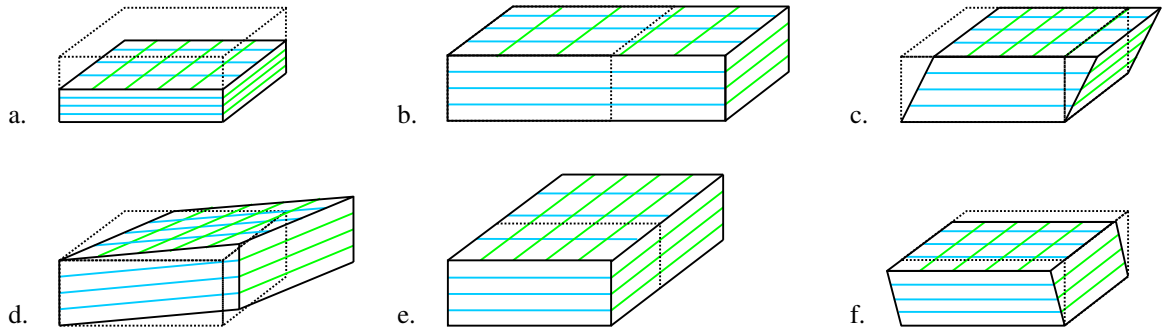

Fig. 3. Deformation modes of layer to layer interlock reinforcements (a) transverse compression, (d) in-plane shear, (b,e) stretches, (c,f) transverse shear.

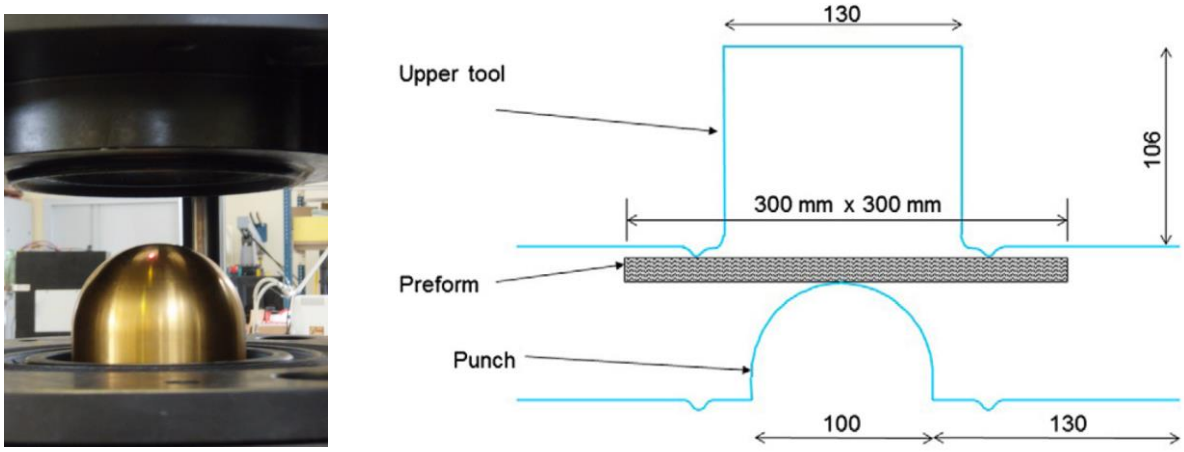

Fig. 4.Hemispherical deep drawing. Geometry of the tolls

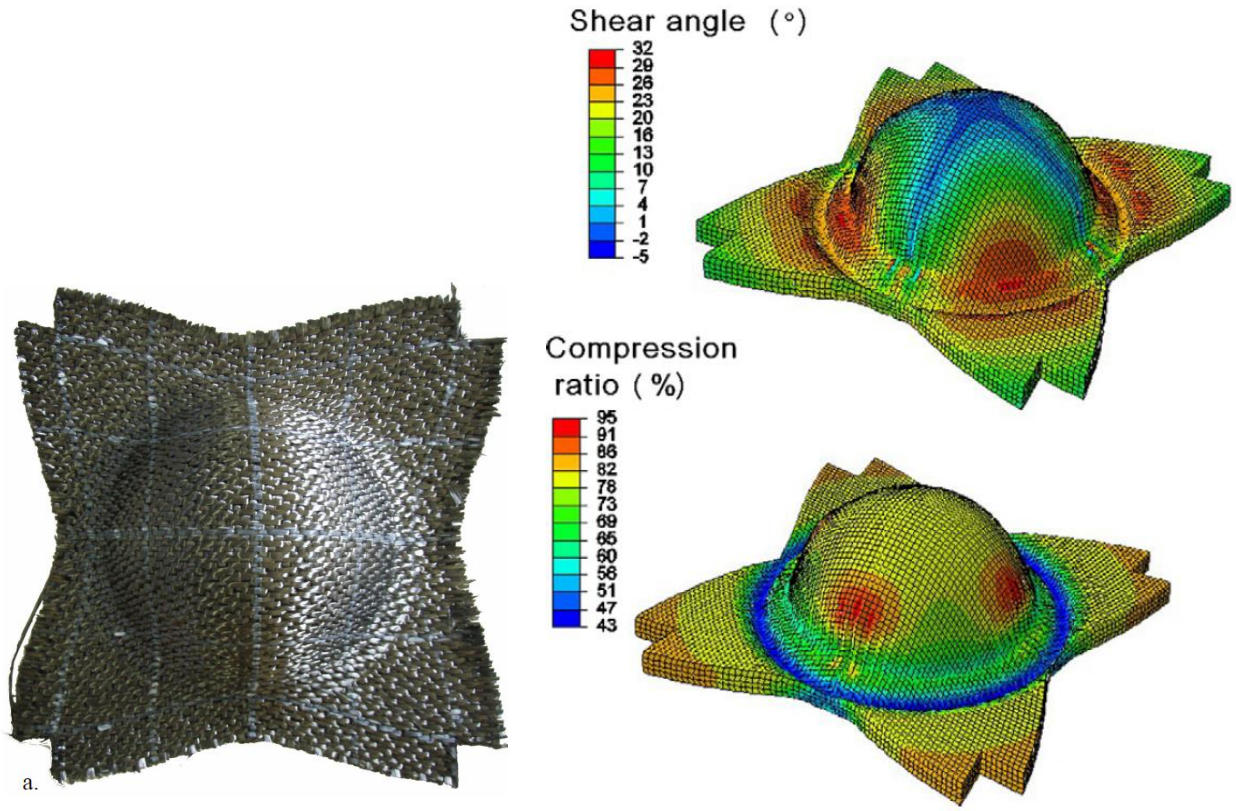

Fig. 5. Hemispherical deep drawing: Experimental deformed shape (left),
Computed shear angles and compaction ratio (right)

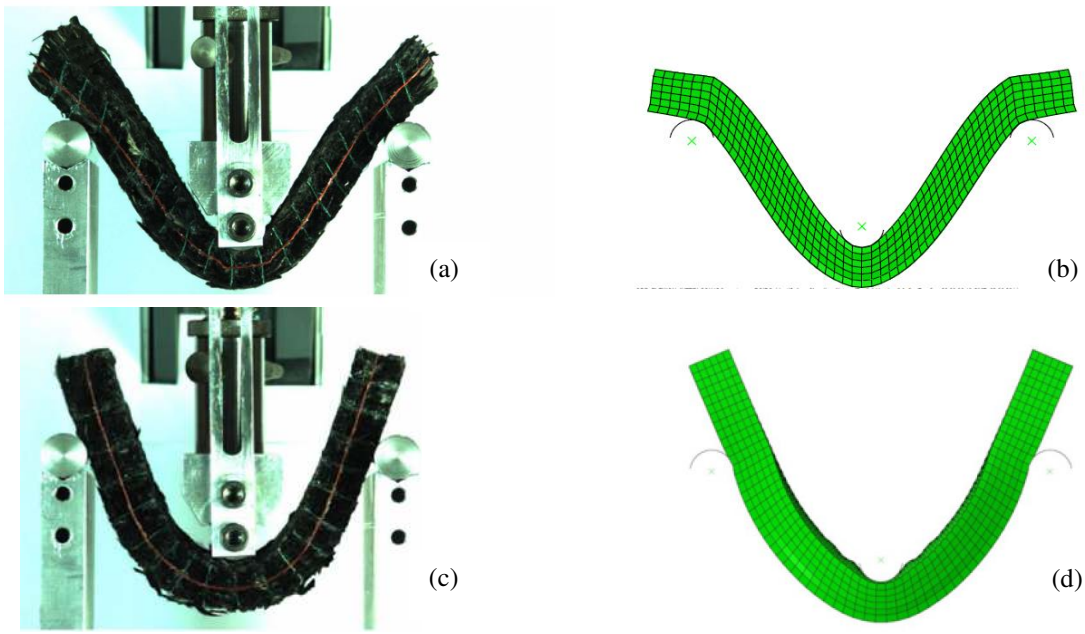

Fig. 6. Interlock three point bending.
Fibres oriented at 0/90° experiments (a) and simulation (b)
Fibres oriented at ±45° experiments (c) and simulation (d)

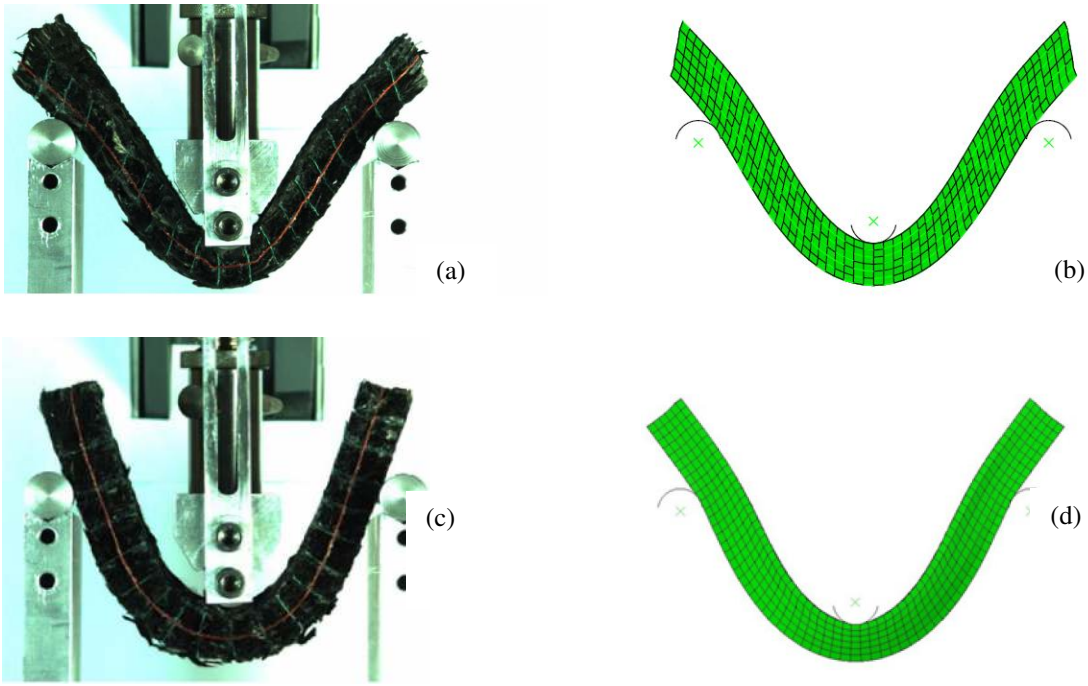

Fig. 7. Interlock three point bending. Simulations with added beams
Fibres oriented at 0/90° experiments (a) and simulation (b)
Fibres oriented at ±45° experiments (c) and simulation (d)

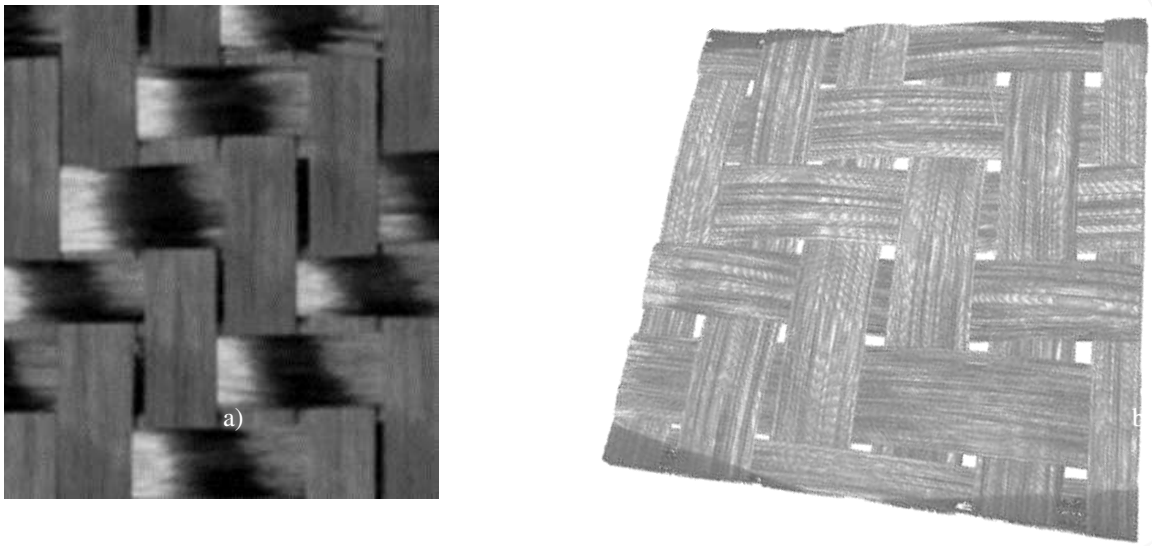

Fig. 8. G986 2x2 carbon twill (left), G986 3D reconstruction from μCT

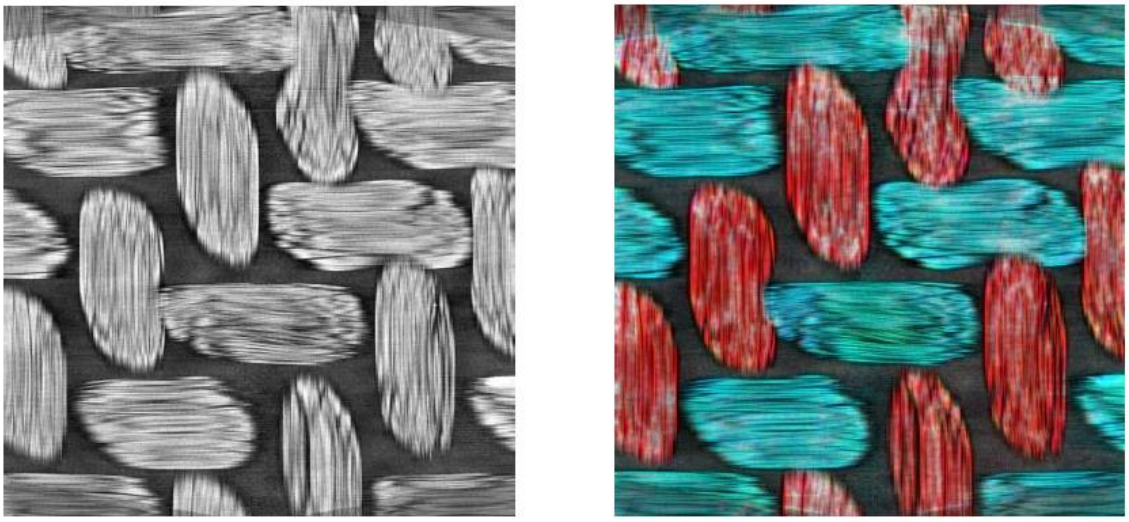

Fig. 9. Tomography cut (left); Separation of warp and weft yarns (right)

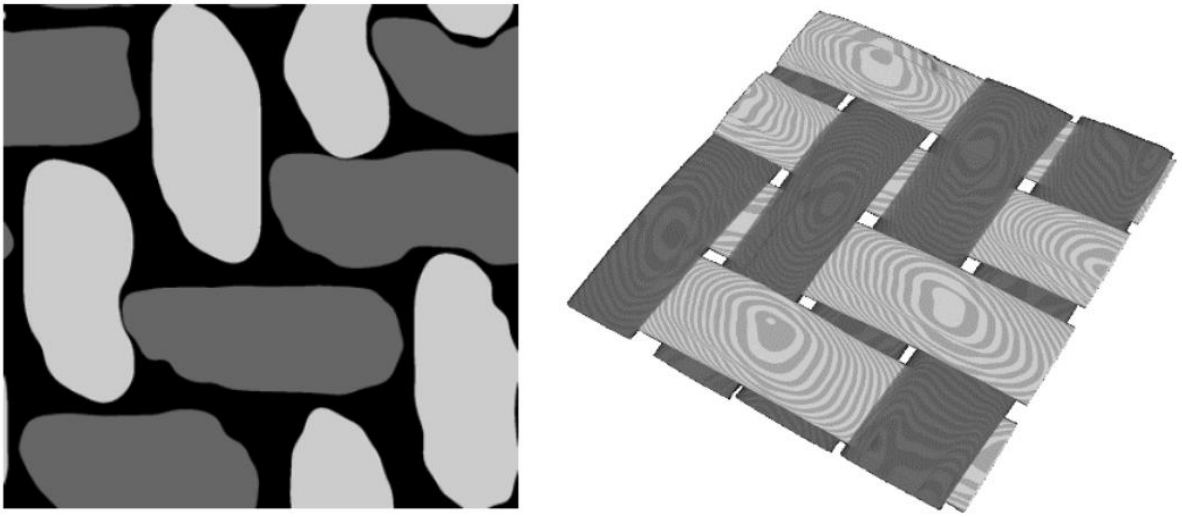

Fig. 10. Grey levels in warp and weft directions (left);
Geometry of the yarns with separated warp and weft yarns (right)

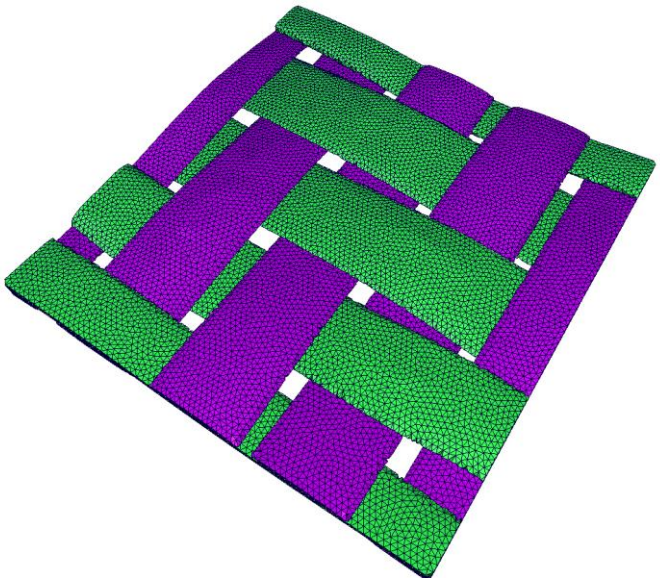

Fig. 11. Tetrahedral mesh obtained from tomography X

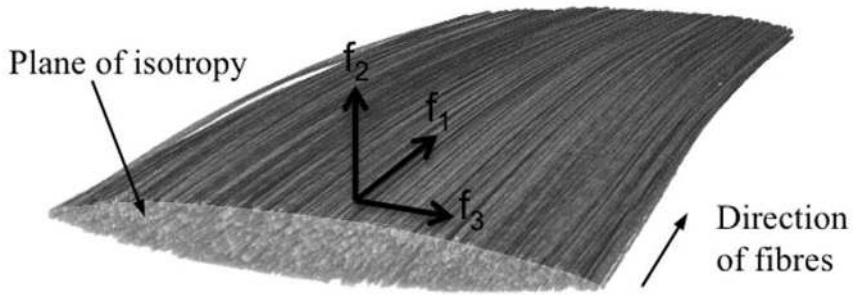

Fig. 12. Direction of the fibres and transverse isotropy

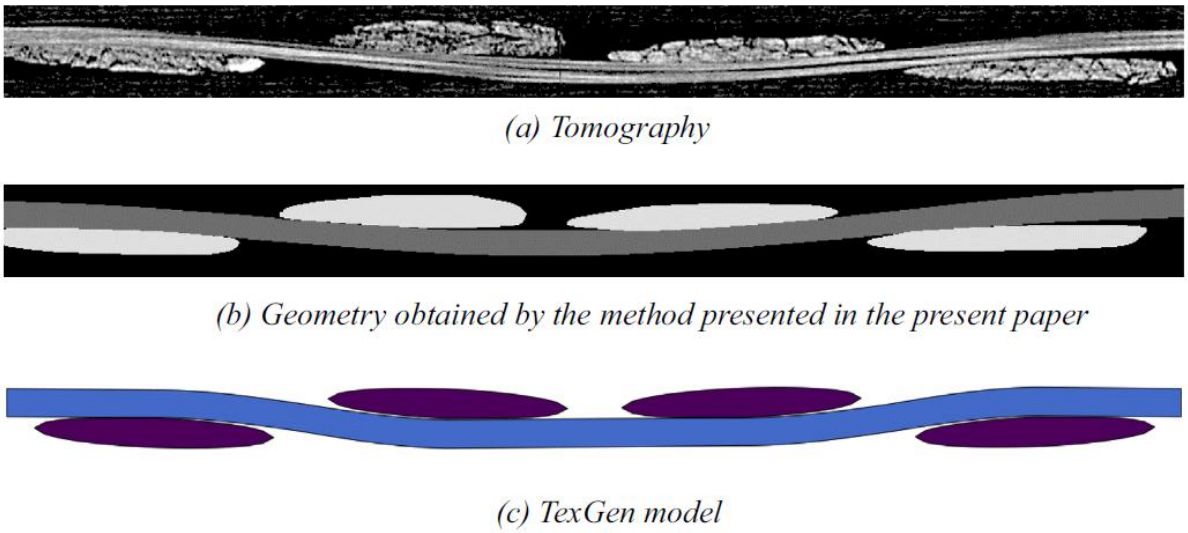

Fig. 13. G986 reinforcement compaction. Comparisons of initial geometries

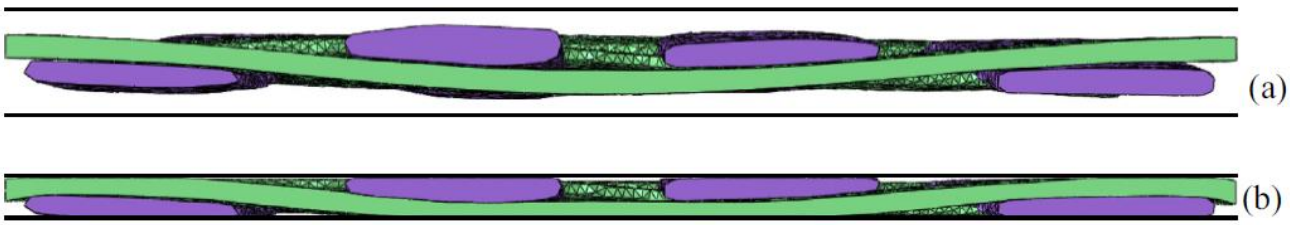

Fig. 14. Simulation of the compaction of a G986 reinforcement. Initial state (a). After compaction (b)

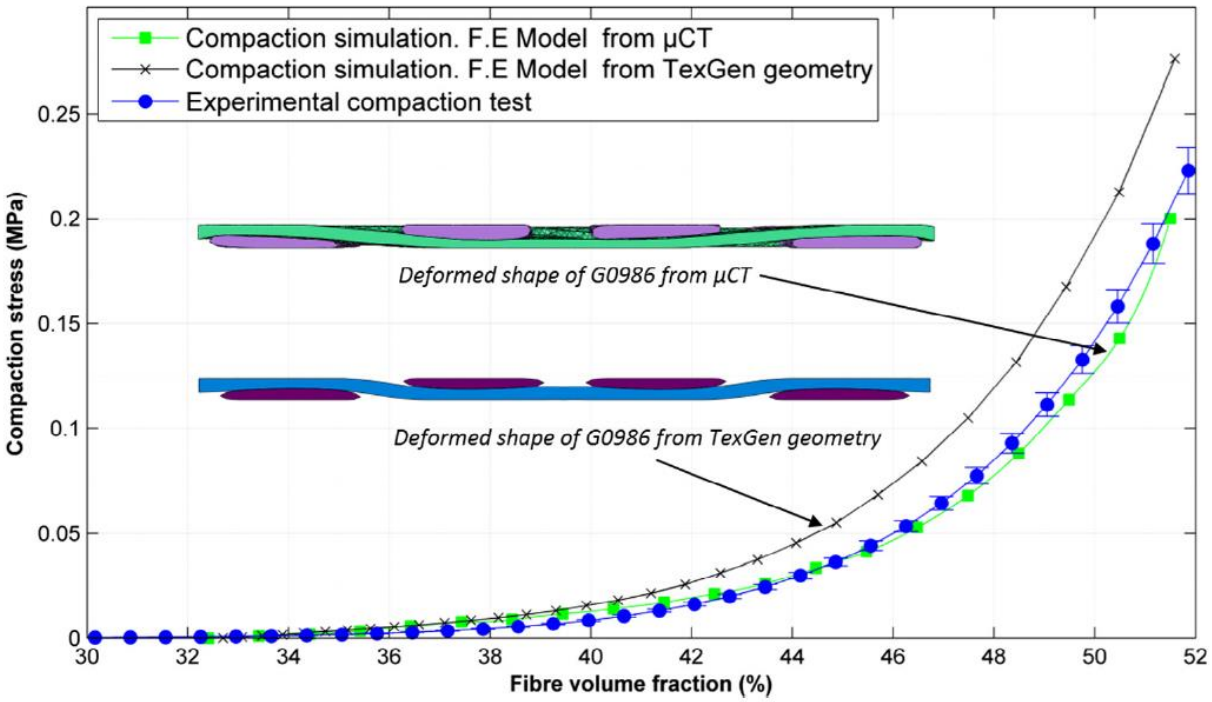

Fig. 15. G986 reinforcement compaction. Comparisons of experiments and simulations